THE JOURNAL OF PHYSICAL CHEMISTRY C

Article

Cite This: J. Phys. Chem. C 2018, 122, 27005−27015

pubs.acs.org/JPCC

Site-Specific Adsorption of CO_2 in Zeolite NaK-A

Przemyslaw Rzepka,[†] Zoltán Bacsik,[†] Stef Smeets,[†] Thomas C. Hansen,[‡] Niklas Hedin,*[,†] and Dariusz Wardecki*[,§,∥]

[†]Department of Materials and Environmental Chemistry, Stockholm University, SE-106 91 Stockholm, Sweden

[‡]Institut Laue-Langevin, 71 Avenue des Martyrs, 38000 Grenoble, France

[§]Institute of Experimental Physics, Faculty of Physics, University of Warsaw, Pasteura 5, 02-093 Warsaw, Poland

[∥]Department of Chemistry and Chemical Engineering, Chalmers University of Technology, SE-412 96 Gothenburg, Sweden

Supporting Information

ABSTRACT: Zeolite $|Na_{12}|$-A is a commercial adsorbent, and its CO_2-over-N_2(CH_4) selectivity can be further enhanced kinetically by replacing Na^+ in the 8-ring windows that control gas diffusion with large cations. In this study, samples of zeolite $|Na_{12-x}K_x|$-A with x = 0.0, 0.8, 2.0, and 3.0 were prepared, and the positions of adsorbed CO_2 molecules were determined using in situ neutron powder diffraction through profile refinement. Adsorbed CO_2 molecules were located at three different sites within the large α-cavities in the zeolite structure, revealing the interaction between the adsorbed CO_2 and the host framework. The number of CO_2 molecules at each site depends on CO_2 pressure and follows site-specific CO_2 isotherms described with a Langmuir model. Most of the CO_2 molecules in zeolite $|Na_{12-x}K_x|$-A bridge two cations at neighboring 8-ring sites. These are relatively weakly physisorbed, and therefore, most of the working capacity of CO_2 adsorption is related to this site. The CO_2 molecules at the second most populated site are coordinated to a cation in the 8-ring plane. Some of them seemed to form chemical bonds with the O atoms of the framework as carbonate-like species and acted as chemisorption. The remaining minor fraction of CO_2 is directly attracted by Na^+ at the 6-rings. The different positioning of physisorbed CO_2 and the presence of chemisorbed CO_2 was confirmed by in situ infrared spectroscopy.

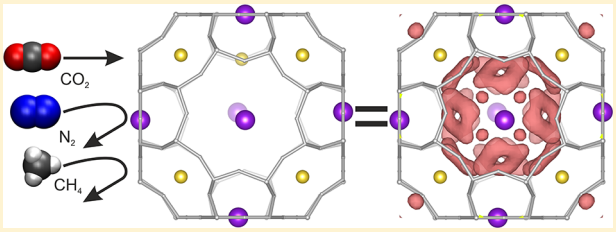

INTRODUCTION

Carbon capture and storage technologies[1] are put forward as a means to limit emissions of CO_2 from combustion of fossil fuels.[2,3] Postcombustion capture of CO_2 can be performed with amine scrubbers, adsorption technologies, membrane processes, or cryogenic separation.[4] Adsorption-driven technologies,[5−7] for example, based on zeolites, have potential economic advantages and can also be used for other CO_2 separation processes such as the upgrading of biomethane,[7,8] which is among the most environmental friendly biofuels.[9]

Separation of CO_2 and N_2 (or CH_4) in adsorption processes can be controlled through both thermodynamics and kinetics. CO_2 has a higher thermodynamic tendency to adsorption than N_2 and CH_4 because of its larger electric quadrupole moment and therefore stronger interactions with the electrical field gradients (EFGs) of adsorbents.[10,11] Moreover, kinetically enhanced CO_2 adsorption can also be related to the so-called effective kinetic diameter in the adsorbed state, which in the case of CO_2 is smaller than for N_2 and CH_4, with estimated values of 0.33 nm for CO_2, 0.36 nm for N_2, and 0.38 nm for CH_4.[12,13] The kinetic effects are significant for adsorbents with effective pore openings in the range of 0.35−0.4 nm. However, it is still under investigation if the additional selectivity of kinetic sorbents can be used for adsorption-driven CO_2 capture or if the mass transfer would be too hampered.

Zeolite $|Na_{12-x}K_x|$-A meets many of the criteria of a CO_2 adsorbent. It has high CO_2 adsorption capacity, high CO_2 selectivity, and robustness; is thermally stable; and can be produced in large quantities at low costs.[13−16] Zeolite A is a small-pore zeolite consisting of a primitive cubic arrangement of large cavities (referred to as the α-cavity) that are joined through common 8-rings forming a three-dimensional channel network. The α-cavities are also joined to $d4r$ units and smaller cages (β-cages) via common 6-rings. The effective size of the 8-ring windows is controlled by the cation in the center of the 8-ring. For Na^+ cations, the effective size of the apertures has been estimated as 0.41 nm,[17,18] which can be decreased by replacing Na^+ with larger monovalent cations[19−21] or increased by replacing Na^+ with Ca^{2+}, Sr^{2+}, or Mg^{2+}.[22−25] For the latter, the 8-ring sites become depopulated. At a critical value of x in $|Na_{12-x}K_x|$-A, sufficiently many pore windows are effectively blocked to hinder the percolation of N_2 or CH_4, which leads to enhanced CO_2 selectivity. With a relatively low value of x, the adsorbent still displays a high CO_2 capacity.[26−30]

The adsorption of CO_2 on $|Na_{12-x}K_x|$-A occurs mainly as physisorption and some as chemisorption. Physisorbed CO_2 molecules interact mainly with their electric quadrupole

Received: September 26, 2018
Revised: October 26, 2018
Published: October 31, 2018

DOI: 10.1021/acs.jpcc.8b09405
J. Phys. Chem. C 2018, 122, 27005−27015

moment to the EFGs of the surface of zeolite.[10,11] Physisorption is the most applicable tool for regular gas separation processes as physisorbed CO_2 can be regenerated more easily than in its chemisorbed forms.[27,31] On several zeolites, physisorption occurs in parallel with chemisorption under which CO_2 reacts and forms (bi)carbonates or similar moieties.[32] However, the mechanism of chemisorption of CO_2 on zeolites has not been well established. The majority of proposed schemes have been derived from IR studies on zeolite X[33−36] and Y[36−38] with mono- and bivalent cations and some from studies on zeolite A.[33,35,39] It has been presumed that the chemisorbed CO_2 couples to O atoms in the framework[34−37] or pulls out one of the O atoms from the framework to form monodentate carbonates.[33,35,37,38] The presence of residual water in the framework can result in the formation of bidentate (bi)carbonates.[37,38]

The mechanism of chemical integration of CO_2 molecules on the surface of zeolites was subject to many structural studies.[5,13,35,40,41] However, until now, the positions of chemisorbed CO_2 molecules in zeolite $|Na_{12-x}K_x|$-A have remained unknown. In a recent study, we used in situ X-ray diffraction to show that the cations were displaced on the adsorption of CO_2 on zeolite $|Na_{12-x}K_x|$-A.[42] However, the X-ray scattering factors for light elements (e.g., C and O) in that study compromised the precision of evaluation of the CO_2 positions in the presence of the heavier scatterers (Na, K). Neutron diffraction provides large enough scattering for C [b = 5.551(2) fm][43] and O [b = 4.232(6) fm],[43] making it more feasible to obtain detailed information on the positioning of CO_2. For example, Hudson et al.[44] and Bae et al.[45] determined the positions of CO_2 molecules on Cu chabazite and zeolite 5A, which lack a cation in the 8-ring window, under different CO_2 loadings using in situ neutron diffraction experiments. In this context, zeolite 5A displays no chemisorption of CO_2 at all.[46]

In this study, we conducted a detailed in situ neutron diffraction study to determine the positions of CO_2 adsorbed on a series of $|Na_{12-x}K_x|$-A compositions and evaluate their quantities through the loading of CO_2. In addition, we tried to directly determine the positions of the chemisorbed CO_2 molecules.

EXPERIMENTAL DETAILS

Synthesis and Experiment. $|Na_{12-x}K_x|$-A samples with x = 0.0, 0.8, 2.0, and 3.0 were prepared from a $|Na_{12}|$-A powder from Luoyang Jianlong Chem. Ind. Co. by ion exchange with KCl following the procedure described in Table S1 in the Supporting Information. The samples consisted of homogeneous cubic particles with an average size of approximately 2.7 μm. The compositions and $K^+/(K^+ + Na^+)$ ratios were determined by elemental analysis with energy-dispersive X-ray spectroscopy (EDS) using a JEOL JSM-7000F scanning electron microscope with zeolite powders spread on ink-coated aluminum stumps. The EDS spectra were collected with 15 keV. The evaluated Si/Al ratio was ∼1:1.

The 0−1000 mbar isotherms of CO_2, N_2, and CH_4 were recorded on a Micromeritics ASAP 2020 surface area and porosity analyzer. Prior to the measurements, the samples were dehydrated for 10 h under high dynamic vacuum (0.001 μbar) at T = 623 K. Then, they were backfilled under 1 bar of dry N_2 at T = 323 K. Afterward, all samples were weighed. The free space in the sample tubes was measured with He gas, which was assumed not to adsorb.[47] The adsorption data on all samples were recorded with a precision of <0.01% during an interval time of 15 s at T = 273 K set and stabilized by an ice bath. The 0.2 mmol/g incremental dosing mode was used to record the low-pressure regime of CO_2 adsorption. Desorption isotherms were measured till 20 kPa. The second-run CO_2 isotherm was recorded on the $|Na_{10}K_2|$-A sample, which had been treated for 12 h under dynamic vacuum (turbopump) at T = 298 K after recording the first-run CO_2 isotherm.

In situ IR spectra were recorded with a Varian 670-IR Fourier transform infrared spectrometer with a liquid nitrogen-cooled mercury cadmium telluride detector. The in situ system consists of a high-vacuum system in stainless steel, a custom-made stainless steel IR transmission cell with KBr windows, which offers possibilities to vary temperature and pressure conditions.[48]

Self-supporting pellets with diameters of 16 mm were made from the zeolites by compacting approximately 25 mg of powder. A pressure of 1 ton/cm^2 was applied for 2 min using a pressing tool. The pellets were dehydrated in the IR transmission cell at low pressure (<10^{-6} mbar) and high temperature (523 K) for typically 6 h. A background IR spectrum was recorded on the dehydrated zeolites; thus, all bands in the presented spectra are related to the adsorption of CO_2. Pure carbon dioxide (>99.9%) was supplied by the Linde Gas Company (AGA) and used as received. Spectra of the gaseous phase were recorded separately at 303 K with only CO_2 present in the cell at the different pressures of CO_2 studied. The corresponding CO_2 reference spectra were subtracted from the absorbance spectra acquired at different CO_2 pressures.

Constant wavelength neutron powder diffraction (NPD) data were collected on the instrument D1B at ILL in Grenoble, France.[49] A series of in situ NPD measurements was performed[50] with the use of a gas stick connected through a stainless steel capillary to the CO_2 gas rig, and a volumetric gas sorption apparatus from Hiden Isochema, as provided by ILLs department for the sample environment. Prior to NPD measurements, the samples were dehydrated ex situ at 623 K under dynamic vacuum of 0.001 μbar for 20 h using the ASAP apparatus, backfilled to a pressure of 1 bar of dry N_2 and sealed in glass flasks with an O-ring cup. NPD measurements, with a wavelength of 2.52 Å, were performed in a range of 2θ: 3−120°, at 273 K. The gas was dosed by a pump controlled by the Hisorp software system with an accuracy of ±1.5 mbar. The $|Na_{12-x}K_x|$-A samples (approximately 3 g each) with x = 0.0, 0.8, 2.0, and 3.0 were packed in aluminum cans with a diameter of 0.8 cm under helium atmosphere in a glovebox and sealed with an indium wire. After mounting the samples to the gas stick and placing them in the beam, they underwent a dehydration process again at 550 K, and under near vacuum conditions of 0.001 μbar for 2 h. After the initial treatment, the samples were cooled down to 273 K and NPD diffraction patterns were measured under the following CO_2 pressures: vacuum (0.001 μbar), 50, 100, 400, 700, and 1000 mbar (Table S4). At the very end, the samples loaded at 1000 mbar were treated under vacuum for 4 h at the same temperature of 273 K, and the NPD patterns were remeasured. The data acquisition time for each scan was 1 h. An empty container was measured for signal subtraction purposes. To obtain the pure NPD signal from the zeolite structure, the Bragg peaks from the aluminum container were subtracted from all data sets. The NPD data were analyzed with the TOPAS 5 program.[51]

DOI: 10.1021/acs.jpcc.8b09405
J. Phys. Chem. C 2018, 122, 27005−27015

RESULTS AND DISCUSSION

Crystal Structure of Dehydrated |$Na_{12-x}K_x$|-A. The crystal structure of dehydrated |$Na_{12-x}K_x$|-A derived from the NPD data was in line with previous neutron[45,52,53] and X-ray diffraction studies.[26,54−57] According to our model, the framework of zeolite |$Na_{12-x}K_x$|-A, described with a cubic unit cell (a = 24.5 Å) and space group $Fm\bar{3}c$, consists of eight large α-cavities encapsulating one β-cage in the center (Figure 1, Table S4 in the Supporting Information). Per large unit cell,

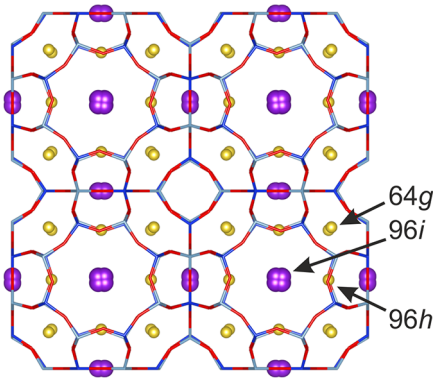

Figure 1. Unit cell of dehydrated |Na_9K_3|-A projected along [1 0 0] with a distribution of extra framework cations: Na^+ (yellow balls) and K^+ (magenta balls). Positions 96*i* and 96*h* are partially occupied.

96 cations are distributed over three sites, where site 64*g*(x, x, x) in the center of the 6-ring is fully occupied. The other two positions, 96*i*(0, y, z) in the 8-ring and 96*h*(1/4, y, y) near the 4-ring, are partially occupied,[54] with occupancies of 0.25 and 0.083, respectively. There is no evidence from the diffraction patterns for the rhombohedral distortion of the framework, seen before in zeolite |Na_{12}|-A.[58,59]

To obtain structural parameters, that is, atomic positions and occupancies for dehydrated compositions of |$Na_{12-x}K_x$|-A, profile refinement[60,61] of the NPD data was performed using the program TOPAS 5.[51] The initial structural parameters were taken from Rzepka et al.[42] The peak shape was modeled using the pseudo-Voigt function. Additional peak asymmetry correction was applied to model the peak shape at low-2θ range. B_{iso} parameters for the nonframework atoms were not refined because of their high correlation with the occupancy factors and set at reasonable values taken from previous studies.[29,42] Profile refinements, for all dehydrated samples, converged with $\chi^2 \approx 4.2$ (Table S4 in the Supporting Information). The small discrepancy between the observed and calculated data can be attributed to unmodeled residual water in the zeolite channels. Representative models and data points are shown in Figure 2a, and the final structural parameters for all samples are listed in Tables S5−S31 in the Supporting Information. Changes in the cation occupancy, as determined from X-ray diffraction studies,[26,42] have shown that during ion exchange, K^+ ions are gradually substituting Na^+ in the 8-ring sites, which eventually leads to a full replacement of Na^+ ions at the 96*i* site in |Na_9K_3|-A. The changes in the cation position in the 8-rings likely relate to the significantly different ionic radii of Na^+ and K^+, with r = 1.16 Å[62] and r = 1.52 Å,[62] respectively. These changes could not be observed in the NPD data directly from differences of the nuclear density in the 8-ring because the neutron scattering lengths for Na and K are very similar: b = 3.63(2) fm and b = 3.67(2) fm, respectively.[43]

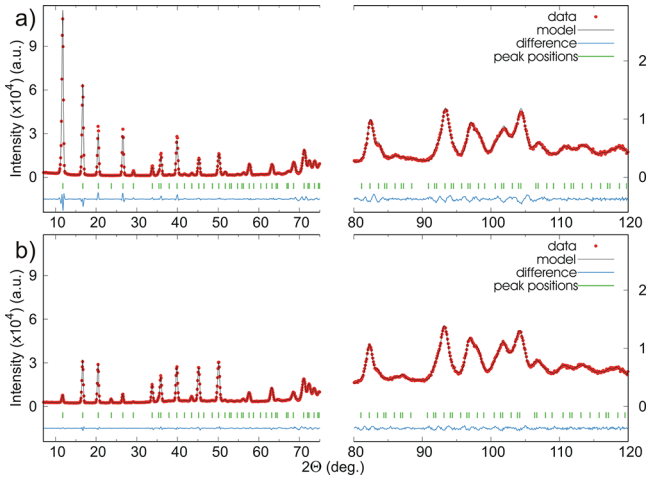

Figure 2. Profile refinements of |Na_9K_3|-A (a) dehydrated and (b) loaded with CO_2 at 1000 mbar and 273 K.

To simplify the model for NPD profile refinement, only one type of cation in the 8-ring was used: Na^+ for x = 0.0 and 0.8 and K^+ for x = 2.0 and 3.0. The refined distances between the cation in the 8-ring and the nearest O atom indeed increased from 2.34(2) Å for |Na_{12}|-A to 3.262(15) Å for |Na_9K_3|-A. Table 1 shows the refined distances between the cation and O(2) for all compositions of |$Na_{12-x}K_x$|-A.

Table 1. Refined Distances Between the 8-Ring Cation (96*i* site) and Nearest Framework O of Different Compositions of Zeolite A Compared to Literature Values

sample	cation−O(2) distance (Å)	reference distance (Å)
|Na_{12}|-A	2.34(2)	2.383(7)[54]
|$Na_{11.2}K_{0.8}$|-A	2.48(11)	
|$Na_{10}K_2$|-A	2.658(3)	
|Na_9K_3|-A	3.262(15)	3.315(10)[55]

Crystallographic Order CO_2 Adsorbed on |$Na_{12-x}K_x$|-A. The relative intensities of the Bragg peaks varied significantly during CO_2 adsorption for all studied compositions. Particularly, the intensity of the first reflection at 2θ = 12° was greatly reduced after loading with CO_2 (cf. Figures 2b and S1−S3). The site preference of the CO_2 molecule in the zeolite framework at different CO_2 pressures was investigated by calculating difference Fourier maps (DFMs) from the NPD data.[63] DFMs were generated for the samples loaded at a CO_2 pressure of 1000 mbar, by taking the difference between the observed and the calculated patterns simulated using only the framework model including the corresponding Na^+/K^+ positions. The initial DFMs revealed the largest peaks in the nuclear density (site I) close to 6-ring, bridging the cations at the neighboring 96*i* sites. Figure 3a,b show the initial DFMs for |Na_{12}|-A and |Na_9K_3|-A, respectively. After placing a CO_2 molecule in the model at that revealed position, a new series of DFMs was generated. This revealed a new peak (site II) situated near the cation at the 96*i* site in the 8-ring. The last CO_2 position (site III) revealed by the DFMs lied along the α-cavity body diagonal, close to the 64*g* site. However, the intensity of this peak was very weak and can possibly also be attributed to residual water or a shift of the cation.

To confirm the CO_2 positions observed in the DFMs, the simulated annealing algorithm implemented in TOPAS 5[64] was

DOI: 10.1021/acs.jpcc.8b09405
J. Phys. Chem. C 2018, 122, 27005−27015

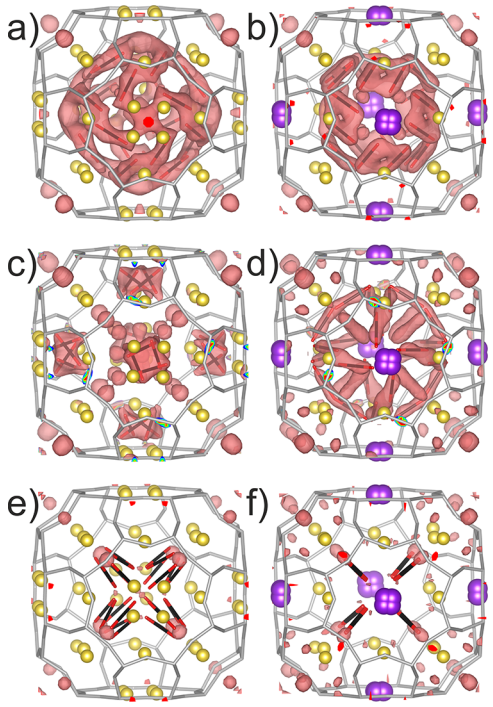

Figure 3. DFMs with corresponding atomic positions (obtained from simulated annealing) of adsorbed CO_2 under 1000 mbar at $|Na_{12}|$-A (left column) and $|Na_9K_3|$-A (right column) for (a,b) site I, (c,d) site II, and (e,f) site III.

used. Simulated annealing is a global optimization algorithm that is particularly well suited for locating organic species inside zeolite frameworks.[65] Expected atoms, molecules, or fragments are placed randomly in the unit cell as rigid bodies and then moved around by modifying their positions, orientations, and free torsion angles. After each rearrangement, the difference between the experimental and calculated profile is evaluated, and the cycle is repeated until convergence is reached. This process is repeated until a satisfactory model fits the data. For this, only the samples loaded at a CO_2 pressure of 1000 mbar were used. Three independent CO_2 molecules were introduced as rigid bodies into the model. The positions, orientations, and occupancies of the CO_2 molecules were then optimized by the simulated annealing algorithm, while keeping all other parameters constant, that is, the positions and occupancies of the framework atoms and cations, as well as the background and profile parameters. Simulated annealing was also attempted with one, two, and four molecules CO_2, but three gave the best agreement with the NPD data. Subsequently, the structure models obtained were refined against the NPD data of the samples loaded at 1000 mbar. These models were then used to initiate subsequent profile refinements for all samples loaded at 700, 400, 100, 50 mbar, and desorbed with vacuum, each time using the refined model of the previous one as input for the next one. Refinements with respect to the data collected at 50−1000 mbar of CO_2 pressure always required three different CO_2 positions.

During the refinements, the following atomic parameters were refined: atomic positions of the framework atoms, atomic position and occupancy of the 6-ring cation, and atomic positions and occupancies of the CO_2 molecules. The peak shape parameters and background were refined as well. The profile parameters and positions of the remaining cations were kept constant in order to improve the stability. The results of refinements for all samples converged with $\chi^2 \approx 1.9-2.9$ and are presented in the Supporting Information.

The positions of the refined CO_2 molecules correspond well to the differential nuclear densities provided by the DFMs (Figures 3 and S4). The discussions below are focused on the two compositions with $x = 0.0$ and 3.0, as the CO_2 positions at the other two investigated compositions ($|Na_{11.2}K_{0.8}|$-A and $|Na_{10}K_2|$-A) were potentially more disordered because of superposition of the CO_2 arrangements related to distributions of K^+ and Na^+.

The CO_2 molecule at site I bridged two cations at neighboring 8-rings (Figure 4a,b) with the O═C═O···Na^+/

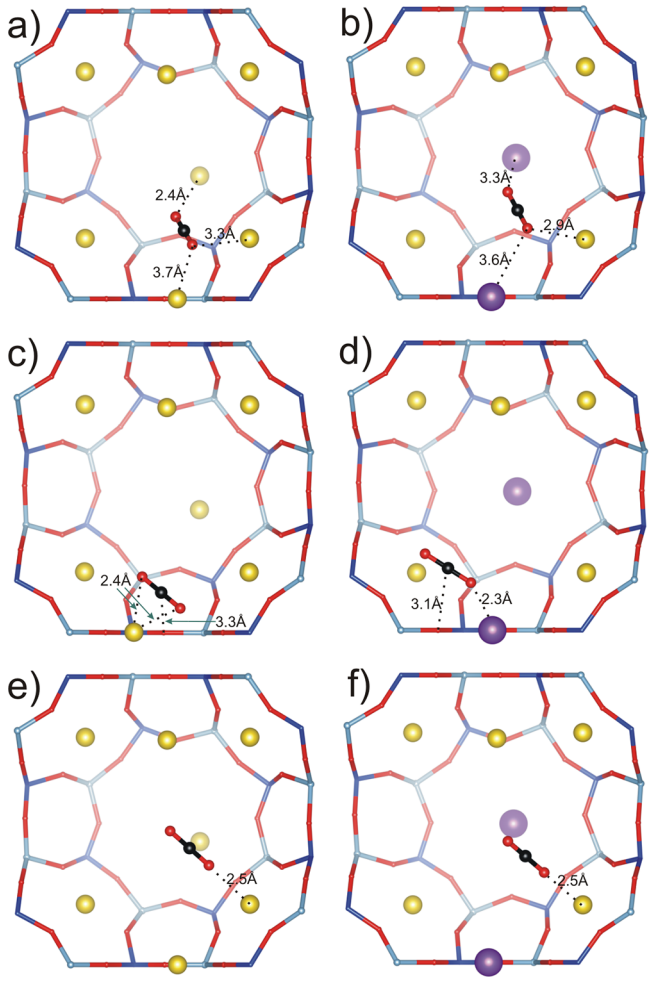

Figure 4. Atomic positions of adsorbed CO_2 under 1000 mbar at $|Na_{12}|$-A (left column) and $|Na_9K_3|$-A (right column), showing the locations of (a,b) site I, (c,d) site II, and (e,f) site III.

K^+ distances of 2.4−3.7 Å for $|Na_{12}|$-A and 3.3−3.6 Å for $|Na_9K_3|$-A, respectively. In addition, the orientation of CO_2 molecules was inclined by attraction to the 6-ring Na^+ with the distance of O═C═O···Na^+ varying between 2.9 and 3.3 Å for different compositions. The CO_2 molecules at site II are coordinated by the cations in the 8-rings, and their positions are different depending on whether they coordinate to Na^+ or K^+. The small Na^+ ions, placed off-center in the 8-ring, allow for the coordination of CO_2 near the plane of the 8-ring (Figure 4c). The larger K^+[62] is placed closer to the center of the 8-ring and appears to have pushed the CO_2 away from the

DOI: 10.1021/acs.jpcc.8b09405
J. Phys. Chem. C 2018, 122, 27005−27015

8-ring plane to a position toward the center of α-cavity (Figure 4d). However, the O═C═O···K^+/Na^+ distances (2.4 Å) and the canting angles between O═C═O and 8-ring plane (35°) are almost identical for both $|Na_{12}|$-A and $|Na_9K_3|$-A. As the closest distances of (C)···O_{ring} are 3.3 Å for Na^+ and 3.1 Å for K^+, the CO_2 molecules at the site II can be interpreted as carbonate-like species as will be discussed later. Moreover, the Na^+ in the 8-ring seems to be interacting with both O atoms of CO_2 at site II (Figure 4c). This configuration is typical for HCO_3^- coordination complexes.[34,35,38] One should note that we opted to model the CO_2, HCO_3^-, or related compounds with the linear CO_2 to reduce the number of parameters in the analyses.

The CO_2 molecules at site III are oriented perpendicularly to the plane of the 6-ring (Figure 4e,f) along the body diagonal. The O atoms are coordinated to Na^+ with an average O═C═O···Na^+ distance of 2.5 Å. The occupancy of this site is low (typically ∼1 molecule per α-cavity), and its very nature is somewhat speculative as discussed before; it can also be assigned to remaining residual water or cation displacement.

CO_2 Physisorption on $|Na_{12-x}K_x|$-A. The CO_2 uptake on $|Na_{12-x}K_x|$-A declined slightly with an increased K^+ content, whereas the CH_4 and N_2 uptakes were basically null for $|Na_{10}K_2|$-A and $|Na_9K_3|$-A (Figure 5). The CO_2 uptake at 1000

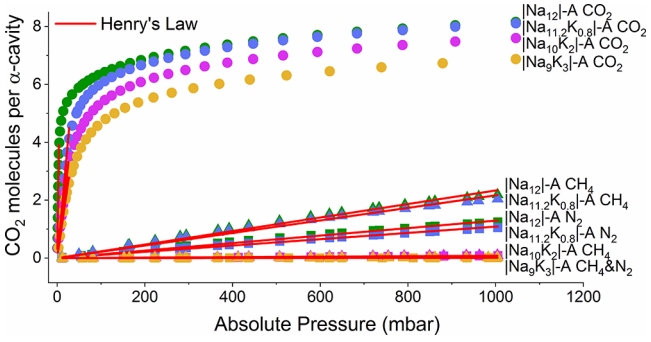

Figure 5. Adsorption isotherms for CO_2, N_2, and CH_4 on $|Na_{12-x}K_x|$-A recorded at 273 K. Regression lines were derived with respect to the all experimental data using a linear Henry's law model.

mbar dropped from 8.2 CO_2 molecules per α-cavity for $|Na_{12}|$-A to 7.1 for $|Na_9K_3|$-A. This effect has been observed previously.[26,27,30] The N_2 and CH_4 isotherms of $|Na_{12}|$-A and $|Na_{11.2}K_{0.8}|$-A can be described over the full range with Henry's law

$$q = K_H p$$

where q is the uptake, K_H is the Henry's law constant (Table S2), and p is the pressure. The CO_2 adsorption conformed to the Henry's law parameters (Table S2) only at low-pressure regimes.[66,67] The selectivity $\alpha(CO_2/N_2(CH_4))$[68,69] was evaluated in the low-pressure regime as

$$\alpha = K_{H_{CO_2}}/K_{H_{N_2(CH_4)}}$$

The compositions with $x \geq 2$ have much higher $\alpha(CO_2/N_2(CH_4))$ values than those with lower x-values (Table 2) as was expected from earlier studies.[26,30] These compositions could be relevant for (kinetically) enhanced adsorptive separation of CO_2.[70−72] The reduced $K_H(N_2,CH_4)$ values are likely related to reduced intracrystalline diffusion. Surprisingly, $|Na_{11.2}K_{0.8}|$-A has smaller $\alpha(CO_2/N_2(CH_4))$ values than $|Na_{12}|$-A, related to the comparably smaller $K_H(CO_2)$. This reduction

Table 2. Selectivity of $|Na_{12-x}K_x|$-A Compositions

sample	CO_2/N_2 selectivity	CO_2/CH_4 selectivity
$\|Na_{12}\|$-A	740	420
$\|Na_{11.2}K_{0.8}\|$-A	160	75
$\|Na_{10}K_2\|$-A	1900	1520
$\|Na_9K_3\|$-A	15 425	6170

was tentatively assigned to the effects of chemisorption of CO_2 (discussed later) or the intracrystalline diffusivity of CO_2.

The structure refinement of the NPD data allowed deriving three site-specific CO_2 adsorption isotherms, and the number of CO_2 molecules at each site per α-cavity is presented in Figure 6 as a function of CO_2 pressure. Analyses of the NPD data provided the total number of CO_2 molecules per α-cavity as ∼10 for $|Na_{12}|$-A and ∼8 for $|Na_9K_3|$-A at a CO_2 pressure of 1 bar. The adsorption isotherms determined from NPD show a higher uptake of CO_2 molecules when compared with volumetric adsorption data [by ∼1 per α-cavity (12%)], which was tentatively ascribed to kinetic effects in the volumetric adsorption experiments related to some contributions of slow diffusion of CO_2 in $|Na_{12-x}K_x|$-A. However, both series follow very similar trends (Figure 6). Irrespective of the compositions, site I was the most populated (with saturation values of 4.6 molecules for $|Na_9K_3|$-A and 5.7 for $|Na_{12}|$-A), followed by site II (with about ∼3 molecules). Site III was only populated with about 1 molecule per α-cavity.

Within the NPD-resolved CO_2 adsorption data, each site-specific isotherm as well as the total number of CO_2 followed Langmuir models. On the other hand, the occupancy of site III was too low to discuss any trend. The shapes of isotherms (in Figure 6) are varied for different sites. CO_2 molecules of site I are further away from the neighboring cations (Figure 4a,b). Hence, they acted more like α-cavity filling than specific adsorption and had a lower slope of the CO_2 isotherm as was expected from the weaker intermolecular interactions. The high slope of the site II adsorption isotherm was ascribed to the proximity of Na^+ and K^+. The chemical integration of CO_2 on the 8-ring Na^+ was greater and more rapid than on K^+ because of the larger Na^+ electric field gradient−CO_2 quadrupole interaction energy ($-\Phi_{FQ}$). $-\Phi_{FQ}$ is known to be nearly proportional to r^{-3} [where: $r = r_i$ (ionic radius) + r_j (radius of adsorbate molecule)].[73]

We also studied the changes in the lattice parameter of zeolite $|Na_{12-x}K_x|$-A on adsorption of CO_2 because some zeolite structures are known to change the lattice constants on adsorption.[45] The unit cells expanded on the adsorption of CO_2 (Figure 7), and the expansions occurred already at low CO_2 pressures, where also CO_2 uptake is high in the corresponding CO_2 adsorption isotherms (cf. Figure 5). The unit cell parameters after evacuation did not restore the initial dimensions (Figure 7), which was related to CO_2 molecules chemisorbed and/or entrapped within the cavities. The observed structure expansion stand in opposition to the structure contraction on CO_2 adsorption reported by Bae et al. for zeolite $|Na_{3.4}Ca_{4.3}|$-A.[45] One should note that zeolite 5A (i.e. $|Na_{3.4}Ca_{4.3}|$-A) has no cations in the 8-ring positions.

The physisorption of CO_2 on the $|Na_{12}|$-A sample was studied with IR spectroscopy. This sample is compositionally simple, and the polarization effect is large for the small Na^+ ions. The latter was expected to have a large effect on the frequencies of the bands for physisorbed CO_2 (at low CO_2 surface coverages). IR spectroscopy has been used to

DOI: 10.1021/acs.jpcc.8b09405
J. Phys. Chem. C 2018, 122, 27005−27015

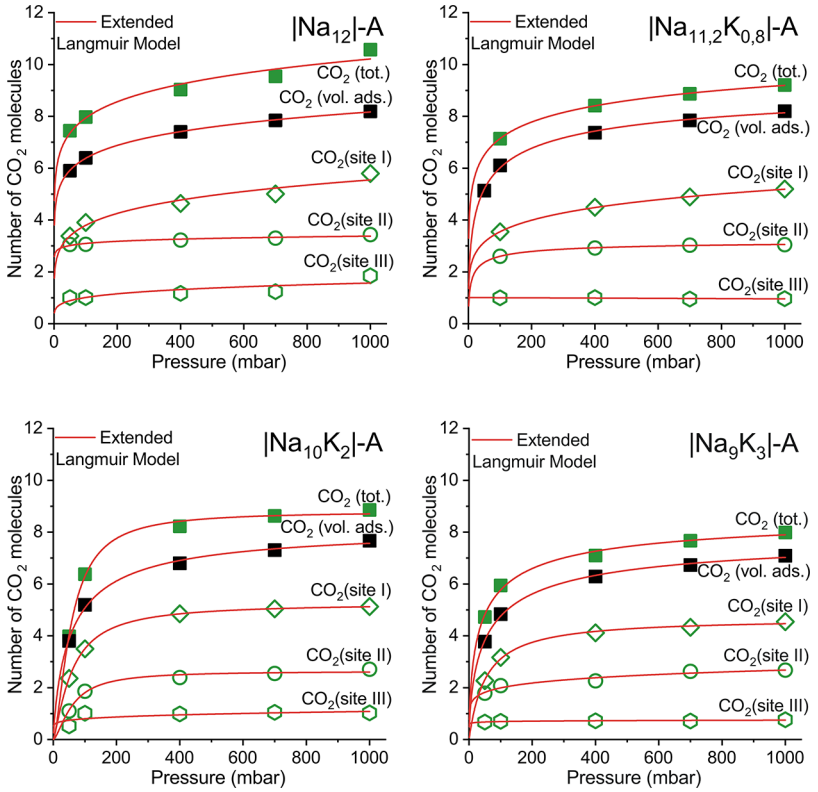

Figure 6. Number of CO_2 positions at $|Na_{12-x}K_x|$-A per α-cavity as a function of CO_2 pressure compared with volumetric adsorption data.

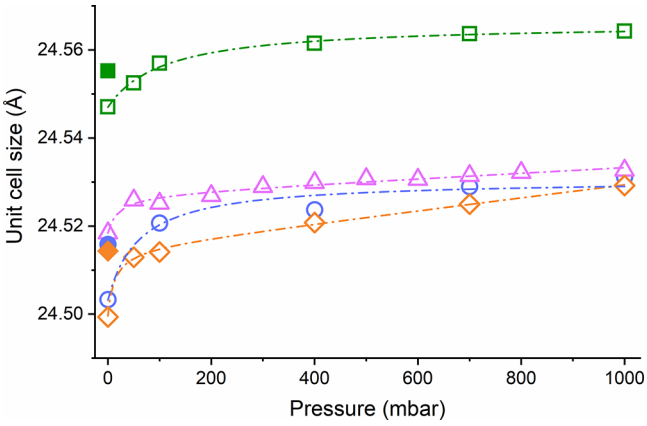

Figure 7. Unit cell expansion during the CO_2 adsorption (open symbols) for $|Na_{12}|$-A (green square), $|Na_{11.2}K_{0.8}|$-A (blue circle), $|Na_{10}K_2|$-A (magenta triangle), and $|Na_9K_3|$-A (orange diamond). Solid symbols correspond to respective unit cell size after desorption.

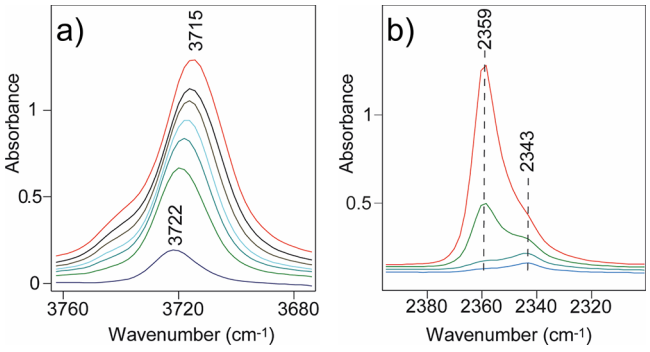

Figure 8. In situ IR spectra of CO_2 adsorbed on (a) $|Na_{12}|$-A, CO_2 combination band during adsorption of CO_2 in the pressure range of 1.33−57 mbar from bottom to top, respectively, and (b) $|Na_{12}|$-A, asymmetric stretching band during desorption with CO_2 pressures of 0.266, 0.095, and 0.004 mbar and in dynamic vacuum after 75 min, respectively, from the top to the bottom.

investigate the interaction of CO_2 and zeolite A[46,74−77] and focused on the CO_2 adsorption at low CO_2 partial pressures (0.1−60 mbar) where CO_2 adsorption is specific in the vicinity of the cations. If the partial pressure of CO_2 is high, the adsorption can be less specific.

The physisorption of CO_2 was studied by a combination band $[(2\nu_2 + \nu_3)$ or $(\nu_3 + \nu_1)]$ and the asymmetric stretching band (ν_3). The combination band was selected as it has a relatively low intensity and is therefore less susceptible to signal saturation. The frequency shift is enhanced by the involvement of different fundamental vibrational modes of CO_2. This band was relatively broad and shifted from 3722 cm^{-1} to lower wavenumbers (Figure 8a) on increasing CO_2 pressure for the adsorption on $|Na_{12}|$-A. These features indicated that different sites or less specific interaction of CO_2 with the charge-balancing cations occurred. Dispersion forces played a role in the adsorption of CO_2 besides of the specific ion−quadrupole moment interactions.

By studying the ν_3 band of CO_2 adsorbed on $|Na_{12}|$-A in the desorption branch (Figure 8b), two distinct bands were clearly detected at 2359 and 2343 cm^{-1}. The band at 2359 cm^{-1} disappeared at higher pressures, and we concluded that the band at 2343 cm^{-1} related to more strongly interacted CO_2. This band was assigned to entrapped physisorbed CO_2 that prevailed with in $|Na_{12}|$-A after long exposure to dynamic high vacuum (IR could not reveal the specific sites in the adsorption branch).

DOI: 10.1021/acs.jpcc.8b09405
J. Phys. Chem. C 2018, 122, 27005−27015

For samples with K^+ ions, $|Na_{12-x}K_x|$-A, the IR spectra are more complex. Cheung et al. showed that the position of the ν_3 band gradually changes with increasing K^+ content,[30] but distinct separated bands were not observed. The entrapped CO_2 had the same frequency as in the case of $|Na_{12}|$-A (spectra are not shown here).

CO_2 Chemisorption on $|Na_{10}K_2|$-A. It has been established that formation of carbonate-like species reduces the second-cycle uptake of CO_2 on zeolite A.[28,30] By contrasting the first-cycle and second-cycle CO_2 adsorption isotherms for $|Na_{10}K_2|$-A, we derived ~0.5 molecule of chemisorbed CO_2 per α-cavity (Figure 9). This composition

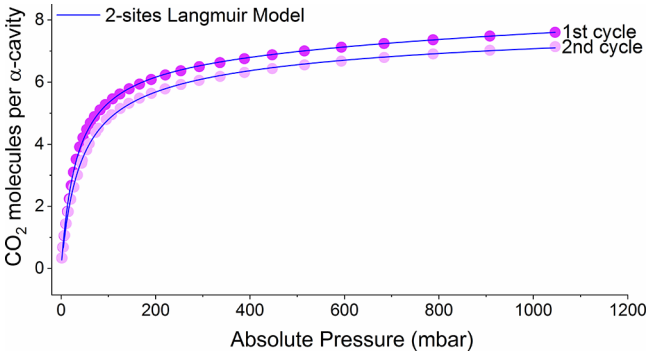

Figure 9. Two cycles of adsorption of CO_2 recorded at $|Na_{10}K_2|$-A at 273 K under high vacuum with 12 h evacuation in between. The data are fitted to the two-site Langmuir model. The difference between the two cycles corresponds to chemisorption of CO_2.

with $x = 2$ was selected because of its high selectivity (cf. Table 2). A single-site Langmuir model cannot be used for CO_2 adsorption on $|Na_{10}K_2|$-A,[45] but a dual-site Langmuir model could represent the data

$$q = \frac{q_{sat_1} b_1 p}{1 + b_1 p} + \frac{q_{sat_2} b_2 p}{1 + b_2 p}$$

with q_{sat1}, q_{sat2}, and b_1, b_2 as the saturation loadings and Langmuir parameters for sites 1 and 2, respectively (Table S3), and p as the equilibrium pressure. This model described the contribution from both chemisorbed and physisorbed species; however, it is empiric and we do not propose q_{sat1} and q_{sat2} to determine physisorbed and chemisorbed amounts. The parameters could also be differentiated by specific sites of adsorption because they were in line with the NDP-resolved adsorption isotherms (cf. Figure 6). The dual-site Langmuir model also needed to be used for the second-cycle CO_2 isotherms, where the influence of chemisorbed CO_2 was smaller.

In situ IR spectra for CO_2 adsorbed in zeolite $|Na_{10}K_2|$-A in a broad CO_2 pressure regime up to 1 bar were recorded and presented in Figure 10. The IR spectra for the CO_2 adsorption branch (Figure 10a) displayed, in addition to the asymmetric stretching (ν_3) mode of physisorbed CO_2 at 2350 cm^{-1}, and intense bands for chemisorbed CO_2 in the region of 1800−1200 cm^{-1}. These bands are typically observed for zeolites with relatively high basicity, like certain compositions of zeolite A, when adsorbing CO_2.[38,46,74,76,78−80] These bands were assigned to carbonates or carbonate-like species, but for such species to form, O atoms need to be transferred either from OH groups acting as acid sites, water, or by reactions with the framework O atoms.[80] Split bands were detected in the spectra

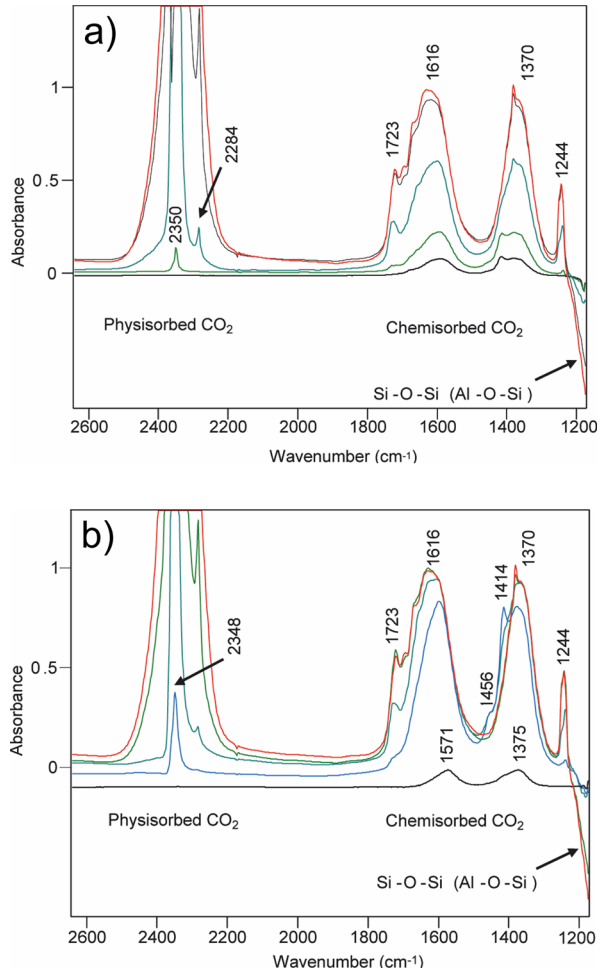

Figure 10. In situ IR spectra of CO_2 adsorbed on (a) zeolite $|Na_{10}K_2|$-A, spectra acquired during adsorption with CO_2 equilibrium pressures of 0.013, 0.260, 12.67, 97, and 1000 mbar, respectively, from bottom to top; (b) zeolite $|Na_{10}K_2|$-A, spectra acquired during desorption with CO_2 equilibrium pressures of 1000, 51, and 0.13 mbar, and after 4 h in dynamic high vacuum, and after heat treatment, respectively, from top to bottom.

instead of a single one that was expected for the doubly degenerated asymmetrical stretching (between 1410 and 1490 cm^{-1}) mode of the symmetrical, planar carbonate. Hence, we concluded that these carbonates are not symmetrical. This broken symmetry of the chemisorbed species was in line with bond formation with the framework. There were for example split bands in the spectra of $|Na_{10}K_2|$-A on CO_2 adsorption at 1723 and 1244 cm^{-1}; 1616 and 1370 cm^{-1}; and 1600 and 1380 cm^{-1}.

The bands for physisorbed CO_2 in the adsorption branch in Figure 10a were most dominant at the highest CO_2 pressure. For example, the overall intensities of the bands for chemisorbed CO_2 were practically the same at 97 and 1000 mbar, but the intensities of the bands for physisorbed CO_2 increased significantly. A negative band was observed at 1175 cm^{-1} and the intensity of this band correlates with the partial pressure of CO_2. Such bands have been observed for $|Na_{12}|$-A[46] and Na-Y[81] in earlier studies and attributed to the perturbation of the framework Si−O−Si (Si−O−Al) modes. The intensity of the band at 1175 cm^{-1} continued to increase even above the CO_2 pressures at which CO_2 stopped to be chemisorbed; therefore, we attributed this band to the perturbation of the

DOI: 10.1021/acs.jpcc.8b09405
J. Phys. Chem. C 2018, 122, 27005−27015

framework modes related to physisorbed CO_2. This assignment was strengthened by the fact that if physisorbed CO_2 is removed by vacuum treatment, this negative band disappears (Figure 10b).

The in situ IR spectra were also recorded along the desorption branch of CO_2 (Figure 10b). As was discussed in relation to Figure 8b, some physisorbed CO_2 had been entrapped and was detected in the spectra under evacuation by dynamic high vacuum. A temperature increase was required to desorb the full fraction of physisorbed CO_2. On the other hand, a minor amount of the chemisorbed species could be removed by reducing the pressure. For example, the split band pair at 1723 and 1244 cm^{-1} probably corresponded to labile carbonate-like or bent CO_2 species[46] and not to bridged carbonates, which could be concluded from the analysis of the extent of this splitting. This showed that not only decreasing pressure (Figure 10b) but also heat regeneration at a moderately high temperature was not enough to remove these carbonates or carbonate-like species. At full vacuum, as well as after heat treatment, the split band pair corresponded to an almost symmetrical carbonate species (possibly CO_3^{2-}) with frequencies of 1456 and 1414 cm^{-1}. The appearance of these bands showed that the system was rather dynamic and that different carbonates can form at different CO_2 surface coverages.

In situ NPD experiments revealed that the re-evacuated samples have different relative Bragg intensities than the dehydrated ones, which is consistent with chemisorbed species or entrapped physisorbed CO_2 (Figure 11). The $|Na_{10}K_2|$-A

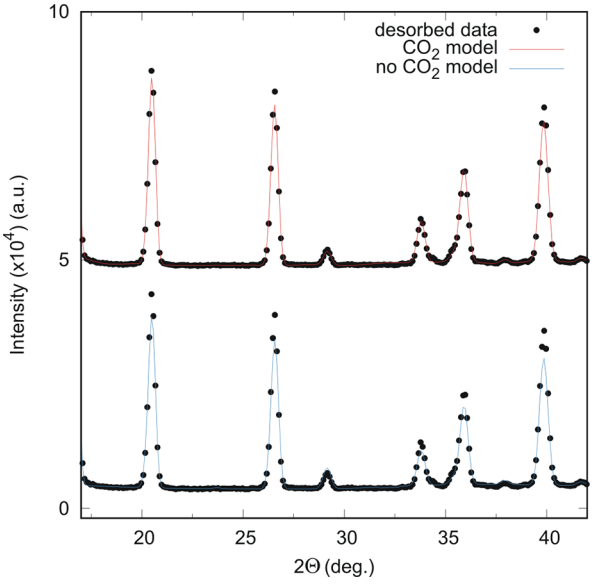

Figure 11. Diffractogram of desorbed $|Na_{10}K_2|$-A under high vacuum for 4 h at 353 K after 1000 mbar CO_2 loading. Collected data compared to structural model with one CO_2 position (site II, ~1 CO_2 molecule per α-cavity) and without CO_2.

was treated at T = 353 K for 4 h of evacuation, which effectively desorbed CO_2 at the amounts observed with volumetric adsorption (cf. Figure 9), indicating that only chemisorbed CO_2 seemed to have remained. The chemisorbed CO_2 molecules in $|Na_{10}K_2|$-A are positioned at site II near the 8-ring, which is corroborated by studies on zeolite 5A,[22] where 8-ring windows remain unoccupied[22] and no chemisorption was detected.[46] In these models, we assumed that the chemisorbed CO_2 could be represented with linear CO_2, and the O═C═O···Na^+/K^+ distance of 2.3 Å corresponded to the respective position under 1000 mbar of CO_2. Furthermore, in the analysis of the chemisorbed CO_2 in $|Na_{10}K_2|$-A subjected to 353 K and 4 h of evacuation, the CO_2 molecules were placed 3.0 Å away from the nearest Na^+ at the 4-ring site. Note that the (C)···O_{ring} distance (3.3 Å) remained smaller than the sum of the van der Waals radii of O and C.[82] Such distancing was used before to describe the interactions of CO_2 with the framework in SSZ-13.[44] Hence, the chemisorbed CO_2 appeared to be bound or coordinated to O in the framework (Figure 12), which is not fully consistent with the IR analysis.

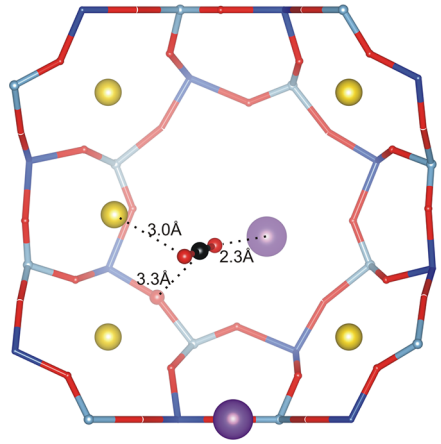

Figure 12. Atomic positions of chemisorbed CO_2 on $|Na_{10}K_2|$-A.

That analysis indicated mainly symmetric carbonate species when the sample was subjected to high dynamic vacuum and/or heat treatment.

The population of site II after desorption was found with the same procedure as CO_2 positions at specific CO_2 pressures, discussed before. However, only one CO_2 position was refined. The occupancy was higher than what would be expected from chemisorbed CO_2 (Table 3). This suggested that only a

Table 3. Number of Molecules of CO_2 Remaining within $|Na_{10}K_2|$-A after 4 h of Evacuation at Dynamic High Vacuum and 353 K[a]

CO_2 pressure (mbar)	site I	site II	site III
1000	5.13	2.71	1.02
0 (desorbed)	0	0.93	0

[a]Corresponding number of molecules in equilibrium with 1000 mbar of CO_2.

fraction of the site II molecules formed CO_3^{2-}/HCO_3^- groups that were retained on desorption. After heat treatment at 353 K and dynamic vacuum, $|Na_{10}K_2|$-A contained ~1 chemisorbed CO_2 molecule per α-cavity, which corresponded to one Na^+ at the 4-ring. We postulate that this cation position plays an important role in the chemisorption. Similar findings have been rationalized by cation gating for related systems.[83,84] Not only chemisorbed CO_2 but also a substantial amount of entrapped physisorbed CO_2 was present in the pores if the evacuation was conducted at T = 273 K (Table S1).

DOI: 10.1021/acs.jpcc.8b09405
J. Phys. Chem. C 2018, 122, 27005−27015

CONCLUSIONS

In situ NPD studies of CO_2 adsorption on $|Na_{12-x}K_x|$-A were used to derive the positions of the adsorbed CO_2 molecules and, for the first time, site-specific CO_2 adsorption isotherms for these structures. The mechanisms of adsorption of CO_2 on zeolite $|Na_{12-x}K_x|$-A were studied in detail, and the in situ NPD experiment revealed three independent sites for the adsorption of CO_2. Adsorbed CO_2 at site I bridges two cations at neighboring 8-rings but also was influenced by Na^+ at 6-ring. The CO_2 adsorption capacity on site I was the highest of the three, but the average cation−CO_2 distance was the longest for this site, which was consistent with the relatively gentle slope for this site I-selective isotherm. The small slope and largest capacity made it relevant to conclude that the working capacity of $|Na_{12-x}K_x|$-A in potential adsorption-driven CO_2 separation processes was mainly related to site I. The CO_2 molecules positioned at site II were coordinated to the 8-ring cations. The mode of CO_2 adsorption was adjusted by the dimensions and positions of Na^+ and K^+ ions in the 8-rings. A fraction (∼1/3) of site II was chemisorbed and appeared to form chemical bonds with the framework of O atoms. These carbonate-like species could not be removed by evacuation under high vacuum, even under moderate heating. The site-selective isotherms of all CO_2 positions conform to a single-component Langmuir model; however, the number of adsorption points was somewhat limited because of experimental constraints.

As was expected from earlier studies, low-K^+ zeolite $|Na_{12-x}K_x|$-A exhibited a high capacity of CO_2 adsorption, and we confirmed earlier findings that tailoring of the pore windows with a sufficient amount of K^+ ($x > 2$) leads to increased $CO_2/N_2(CH_4)$ selectivities. However, we also showed that for compositions with $x = 0.8$, a small amount of K^+, the $CO_2/N_2(CH_4)$ selectivity was actually smaller than for $x = 0$ ($|Na_{12}|$-A). Further studies on the positioning of CO_2 and mode of adsorption (chemisorption/physisorption) on $|Na_{12-x}K_x|$-A and similar compounds are key to reveal the detailed chemistry and physical interplay occurring on these sorbents.

ASSOCIATED CONTENT

Supporting Information

The Supporting Information is available free of charge on the ACS Publications website at DOI: 10.1021/acs.jpcc.8b09405.

> Ion exchange procedure; parameters of Henry's law models for the adsorption of CO_2, N_2, and CH_4 on all investigated compositions; parameters of the dual-site Langmuir models for the first and second cycle of adsorption of CO_2 on $|Na_{10}K_2|$-A; atomic positions, occupancies, and displacements for all samples; selected interatomic distances and angles; NPD profiles for all samples; Fourier maps of extra framework cations; and CO_2 for all samples (PDF)

AUTHOR INFORMATION

Corresponding Authors

*E-mail: niklas.hedin@mmk.su.se (N.H.).
*E-mail: wardecki@chalmers.se (D.W.).

ORCID

Przemyslaw Rzepka: 0000-0003-3185-3535
Stef Smeets: 0000-0002-5413-9038
Thomas C. Hansen: 0000-0003-4611-2393
Niklas Hedin: 0000-0002-7284-2974
Dariusz Wardecki: 0000-0001-6458-3987

Notes

The authors declare the following competing financial interest(s): N.H. is a cofounder and co-owner of SIA NeoZeo commercializing adsorption-driven biogas upgrading.

ACKNOWLEDGMENTS

The research was financially supported by the Swedish Energy Agency, the Swedish Research Council (VR), and the Swedish Governmental Agency for Innovation Systems (VINNOVA) through the Berzelii Center EXSELENT. We would like to acknowledge of the Institut Laue-Langevin (ILL) where the in situ experiments were performed at the high-intensity ND beamline D1B and Dr. Vivian Nassif for her help with setting up the experiment, as well as Simon Baudoin for the setup of the gas adsorption system. We would also like to thank Amber Mace for fruitful discussions about intermolecular interactions. S.S. thanks the Swiss National Science Foundation for financial support (project number: 177761).

REFERENCES

(1) Haszeldine, R. S. Carbon Capture and Storage: How Green Can Black Be? *Science* **2009**, *325*, 1647−1652.
(2) Moss, R. H.; Edmonds, J. A.; Hibbard, K. A.; Manning, M. R.; Rose, S. K.; van Vuuren, D. P.; Carter, T. R.; Emori, S.; Kainuma, M.; Kram, T.; et al. The Next Generation of Scenarios for Climate Change Research and Assessment. *Nature* **2010**, *463*, 747−756.
(3) Root, T. L.; Price, J. T.; Hall, K. R.; Schneider, S. H.; Rosenzweig, C.; Pounds, J. A. Fingerprints of Global Warming on Wild Animals and Plants. *Nature* **2003**, *421*, 57−60.
(4) Leung, D. Y. C.; Caramanna, G.; Maroto-Valer, M. M. An Overview of Current Status of Carbon Dioxide Capture and Storage Technologies. *Renewable Sustainable Energy Rev.* **2014**, *39*, 426−443.
(5) Choi, S.; Drese, J. H.; Jones, C. W. Adsorbent Materials for Carbon Dioxide Capture from Large Anthropogenic Point Sources. *ChemSusChem* **2009**, *2*, 796−854.
(6) Hasan, M. M. F.; First, E. L.; Floudas, C. A. Cost-effective CO_2 capture based on in silico screening of zeolites and process optimization. *Phys. Chem. Chem. Phys.* **2013**, *15*, 17601−17618.
(7) Webley, P. A. Adsorption technology for CO_2 separation and capture: a perspective. *Adsorption* **2014**, *20*, 225−231.
(8) Duan, J.; Jin, W.; Krishna, R. Natural Gas Purification Using a Porous Coordination Polymer with Water and Chemical Stability. *Inorg. Chem.* **2015**, *54*, 4279−4284.
(9) Edwards, R.; Hass, H.; Larivé, J.-F.; Lonza, L.; Mass, H.; Rickeard, D.; Larive, J.-F.; Rickeard, D.; Weindorf, W. *Well-to-Wheels Analysis of Future Automotive Fuels and Powertrains in the European Context WELL-TO-TANK (WTT) Report*, version 4, 2014.
(10) Graham, C.; Pierrus, J.; Raab, R. E. Measurement of the electric quadrupole moments of CO_2, CO and N_2. *Mol. Phys.* **1989**, *67*, 939−955.
(11) Graham, C.; Imrie, D. A.; Raab, R. E. Measurement of the electric quadrupole moments of CO_2, CO, N_2, Cl_2 and BF_3. *Mol. Phys.* **1998**, *93*, 49−56.
(12) Weast, R.; Astle, M.; Beyer, W. *CRC Handbook of Chemistry and Physics*; CRC Press, 1989.
(13) Cheung, O.; Hedin, N. Zeolites and related sorbents with narrow pores for CO_2 separation from flue gas. *RSC Adv.* **2014**, *4*, 14480−14494.
(14) D'Alessandro, D. M.; Smit, B.; Long, J. R. Carbon Dioxide Capture: Prospects for New Materials. *Angew. Chem., Int. Ed.* **2010**, *49*, 6058−6082.

DOI: 10.1021/acs.jpcc.8b09405
J. Phys. Chem. C 2018, 122, 27005−27015

(15) Hedin, N.; Andersson, L.; Bergström, L.; Yan, J. Adsorbents for the post-combustion capture of CO_2 using rapid temperature swing or vacuum swing adsorption. *Appl. Energy* **2013**, *104*, 418−433.
(16) Hedin, N.; Chen, L.; Laaksonen, A. Sorbents for CO_2 capture from flue gas-aspects from materials and theoretical chemistry. *Nanoscale* **2010**, *2*, 1819−1841.
(17) Grämlich, V.; Meier, W. M. The crystal structure of hydrated NaA: A detailed refinement of a pseudosymmetric zeolite structure. *Z. Kristallogr., Kristallgeom., Kristallphys., Kristallchem.* **1971**, *133*, 134−149.
(18) Kim, H.; Cho, H. S.; Kim, C.; Choi, M. Gradual Disordering of LTA Zeolite for Continuous Tuning of the Molecular Sieving Effect. *J. Phys. Chem. C* **2017**, *121*, 6807−6812.
(19) Hedin, N.; DeMartin, G. J.; Strohmaier, K. G.; Reyes, S. C. PFG NMR Self-Diffusion of Propylene in ITQ-29, CaA and NaCaA: Window Size and Cation Effects. *Microporous Mesoporous Mater.* **2007**, *98*, 182−188.
(20) Price, L.; Leung, K.; Sartbaeva, A. Local and Average Structural Changes in Zeolite A upon Ion Exchange. *Magnetochemistry* **2017**, *3*, 42.
(21) Sun, H.; Wu, D.; Liu, K.; Guo, X.; Navrotsky, A. Energetics of Alkali and Alkaline Earth Ion-Exchanged Zeolite A. *J. Phys. Chem. C* **2016**, *120*, 15251−15256.
(22) Pluth, J. J.; Smith, J. V. Crystal structure of dehydrated calcium-exchanged zeolite A. Absence of near-zero-coordinate Ca^{2+} ion. Presence of aluminum complex. *J. Am. Chem. Soc.* **1983**, *105*, 1192−1195.
(23) Pluth, J. J.; Smith, J. V. Crystal structure of dehydrated potassium-exchanged Zeolite A. Absence of supposed zero-coordinated potassium. Refinement of silicon, aluminum-ordered superstructure. *J. Phys. Chem.* **1979**, *83*, 741−749.
(24) Firor, R. L.; Seff, K. Near zero coordinate Ca^{2+} and Sr^{2+} in zeolite A. Crystal structures of dehydrated Ca6-A and Sr6-A. *J. Am. Chem. Soc.* **1978**, *100*, 3091−3096.
(25) Adams, J. M.; Rees, L. V. C. The structure of a dehydrated partially magnesium exchanged zeolite a ($\sim Mg_2Na_8A$) by neutron profile refinement. *J. Solid State Chem.* **1986**, *62*, 184−190.
(26) Liu, Q.; Mace, A.; Bacsik, Z.; Sun, J.; Laaksonen, A.; Hedin, N. NaKA sorbents with high CO_2-over-N_2 selectivity and high capacity to adsorb CO_2. *Chem. Commun.* **2010**, *46*, 4502−4504.
(27) Bacsik, Z.; Cheung, O.; Vasiliev, P.; Hedin, N. Selective separation of CO_2 and CH_4 for biogas upgrading on zeolite NaKA and SAPO-56. *Appl. Energy* **2016**, *162*, 613−621.
(28) Cheung, O.; Bacsik, Z.; Krokidas, P.; Mace, A.; Laaksonen, A.; Hedin, N. K^+ Exchanged Zeolite ZK-4 as a Highly Selective Sorbent for CO_2. *Langmuir* **2014**, *30*, 9682−9690.
(29) Cheung, O.; Wardecki, D.; Bacsik, Z.; Vasiliev, P.; McCusker, L. B.; Hedin, N. Highly selective uptake of carbon dioxide on the zeolite $|Na_{10.2}KCs_{0.8}|$-LTA - a possible sorbent for biogas upgrading. *Phys. Chem. Chem. Phys.* **2016**, *18*, 16080−16083.
(30) Cheung, O.; Bacsik, Z.; Liu, Q.; Mace, A.; Hedin, N. Adsorption kinetics for CO_2 on highly selective zeolites NaKA and nano-NaKA. *Appl. Energy* **2013**, *112*, 1326−1336.
(31) Palomino, M.; Corma, A.; Rey, F.; Valencia, S. New Insights on CO_2−Methane Separation Using LTA Zeolites with Different Si/Al Ratios and a First Comparison with MOFs. *Langmuir* **2010**, *26*, 1910−1917.
(32) Satyapal, S.; Filburn, T.; Trela, J.; Strange, J. Performance and Properties of a Solid Amine Sorbent for Carbon Dioxide Removal in Space Life Support Applications. *Energy Fuels* **2001**, *15*, 250−255.
(33) Amari, D.; Lopez Cuesta, J. M.; Nguyen, N. P.; Jerrentrup, R.; Ginoux, J. L. Chemisorption and physisorption of CO_2 on cation exchanged zeolitesA, X and mor. *J. Therm. Anal.* **1992**, *38*, 1005−1015.
(34) Jacobs, P. A.; van Cauwelaert, F. H.; Vansant, E. F.; Uytterhoeven, J. B. Surface probing of synthetic faujasites by adsorption of carbon dioxide. Part 1.-Infra-red study of carbon dioxide adsorbed on Na-Ca-Y and Na-Mg-Y zeolites. *J. Chem. Soc., Faraday Trans. 1* **1973**, *69*, 1056−1068.
(35) Siriwardane, R. V.; Shen, M.-S.; Fisher, E. P.; Losch, J. Adsorption of CO_2 on Zeolites at Moderate Temperatures. *Energy Fuels* **2005**, *19*, 1153−1159.
(36) Bonenfant, D.; Kharoune, M.; Niquette, P.; Mimeault, M.; Hausler, R. Advances in Principal Factors Influencing Carbon Dioxide Adsorption on Zeolites. *Sci. Technol. Adv. Mater.* **2008**, *9*, 013007.
(37) Gallei, E.; Stumpf, G. Infrared Spectroscopic Studies of the Adsorption of Carbon Dioxide and the Coadsorption of Carbon Dioxide and Water on CaY- and NiY-Zeolites. *J. Colloid Interface Sci.* **1976**, *55*, 415−420.
(38) Jacobs, P. A.; van Cauwelaert, F. H.; Vansant, E. F.; Uytterhoeven, J. B. Surface probing of synthetic faujasites by adsorption of carbon dioxide. Part 1.-Infra-red study of carbon dioxide adsorbed on Na-Ca-Y and Na-Mg-Y zeolites. *J. Chem. Soc., Faraday Trans. 1* **1973**, *69*, 1056−1068.
(39) Larin, A. V.; Mace, A.; Rybakov, A. A.; Laaksonen, A. Carbonate "door" in the NaKA zeolite as the reason of higher CO_2 uptake relative to N_2. *Microporous Mesoporous Mater.* **2012**, *162*, 98−104.
(40) Li, Y.; Yi, H.; Tang, X.; Li, F.; Yuan, Q. Adsorption separation of CO_2/CH_4 gas mixture on the commercial zeolites at atmospheric pressure. *Chem. Eng. J.* **2013**, *229*, 50−56.
(41) Moliner, M.; Martínez, C.; Corma, A. Synthesis Strategies for Preparing Useful Small Pore Zeolites and Zeotypes for Gas Separations and Catalysis. *Chem. Mater.* **2014**, *26*, 246−258.
(42) Rzepka, P.; Wardecki, D.; Smeets, S.; Müller, M.; Gies, H.; Zou, X.; Hedin, N. CO_2-Induced Displacement of Na^+ and K^+ in Zeolite | NaKl-A. *J. Phys. Chem. C* **2018**, *122*, 17211−17220.
(43) Dianoux, A. J.; Lander, G.; Börner, H.; Brown, J.; Carlile, C. J.; Cubitt, R.; Currat, R.; Farago, B.; Hewat, A.; Kulda, J.; et al. *Neutron Data Booklet*, 2003.
(44) Hudson, M. R.; Queen, W. L.; Mason, J. A.; Fickel, D. W.; Lobo, R. F.; Brown, C. M. Unconventional, Highly Selective CO_2 Adsorption in Zeolite SSZ-13. *J. Am. Chem. Soc.* **2012**, *134*, 1970−1973.
(45) Bae, T.-H.; Hudson, M. R.; Mason, J. A.; Queen, W. L.; Dutton, J. J.; Sumida, K.; Micklash, K. J.; Kaye, S. S.; Brown, C. M.; Long, J. R. Evaluation of Cation-Exchanged Zeolite Adsorbents for Post-Combustion Carbon Dioxide Capture. *Energy Environ. Sci.* **2013**, *6*, 128−138.
(46) Montanari, T.; Busca, G. On the mechanism of adsorption and separation of CO_2 on LTA zeolites: An IR investigation. *Vib. Spectrosc.* **2008**, *46*, 45−51.
(47) Finkelstein, Y.; Saig, A.; Danon, A.; Koresh, J. E. Study of Type-A Zeolites. Part 1: Mechanism of He and Ne Encapsulation. *J. Phys. Chem. B* **2003**, *107*, 9170−9174.
(48) Bacsik, Z.; Atluri, R.; Garcia-Bennett, A. E.; Hedin, N. Temperature-Induced Uptake of CO_2 and Formation of Carbamates in Mesocaged Silica Modified with n-Propylamines. *Langmuir* **2010**, *26*, 10013−10024.
(49) Orench, I. P.; Clergeau, J. F.; Martínez, S.; Olmos, M.; Fabelo, O.; Campo, J. The New Powder Diffractometer D1B of the Institut Laue Langevin. *J. Phys.: Conf. Ser.* **2014**, *549*, 012003.
(50) Wardecki, D.; Thomas, H.; Niklas, H.; Laetitia, L.; Vivian, N.; Przenioslo, R.; Rzepka, P. CO_2 capture on Zeolite A and ZK4 with various non-framework cation compositions. https://doi.ill.fr/10.5291/ILL-DATA.5-23-690 (accessed Sep 21, 2018).
(51) Coelho, A. A. TOPAS and TOPAS-Academic: an optimization program integrating computer algebra and crystallographic objects written in C++. *J. Appl. Crystallogr.* **2018**, *51*, 210−218.
(52) Cheetham, A. K.; Eddy, M. M.; Jefferson, D. A.; Thomas, J. M. A study of Si,Al ordering in thallium zeolite-A by powder neutron diffraction. *Nature* **1982**, *299*, 24−26.
(53) Adams, J. M.; Haselden, D. A.; Hewat, A. W. The Structure of Dehydrated Na Zeolite A (Si/Al = 1.09) by Neutron Profile Refinement. *J. Solid State Chem.* **1982**, *44*, 245−253.
(54) Pluth, J. J.; Smith, J. V. Accurate redetermination of crystal structure of dehydrated zeolite A. Absence of near zero coordination

DOI: 10.1021/acs.jpcc.8b09405
J. Phys. Chem. C 2018, 122, 27005−27015

of sodium. Refinement of silicon, aluminum-ordered superstructure. *J. Am. Chem. Soc.* **1980**, *102*, 4704−4708.
(55) Pluth, J. J.; Smith, J. V. Crystal Structure of Dehydrated Potassium-Exchanged Zeolite A. Absence of Supposed Zero-Coordinated Potassium. Refinement of Silicon, Aluminum-Ordered Superstructure. *J. Phys. Chem.* **1979**, *83*, 741−749.
(56) Subramanian, V.; Seff, K. A near zero coordinate sodium ion in dehydrated zeolite 4A, Na_{12}-A. *J. Phys. Chem.* **1977**, *81*, 2249−2251.
(57) Leung, P. C. W.; Kunz, K. B.; Seff, K.; Maxwell, I. E. Crystal Structures of Hydrated and Dehydrated Potassium-Exchanged Zeolite A. *J. Phys. Chem.* **1975**, *79*, 2157−2162.
(58) Thomas, J. M.; Bursill, L. A.; Lodge, E. A.; Cheetham, A. K.; Fyfe, C. A. A Reassessment of Zeolite A: Evidence That the Structure Is Rhombohedral with Unexpected Ordering in the Aluminosilicate Framework. *J. Chem. Soc., Chem. Commun.* **1981**, 276−277.
(59) Bursill, L. A.; Lodge, E. A.; Thomas, J. M.; Cheetham, A. K. New Light on the Crystal Structure of Zeolite A. *J. Phys. Chem.* **1981**, *85*, 2409−2421.
(60) Rietveld, H. M. A Profile Refinement Method for Nuclear and Magnetic Structures. *J. Appl. Crystallogr.* **1969**, *2*, 65−71.
(61) Loopstra, B. O.; Rietveld, H. M. The Structure of Some Alkaline-Earth Metal Uranates. *Acta Crystallogr., Sect. B: Struct. Crystallogr. Cryst. Chem.* **1969**, *25*, 787−791.
(62) Shannon, R. D. Revised Effective Ionic Radii and Systematic Studies of Interatomic Distances in Halides and Chalcogenides. *Acta Crystallogr., Sect. A: Cryst. Phys., Diffr., Theor. Gen. Crystallogr.* **1976**, *32*, 751−767.
(63) Henderson, R.; Moffat, J. K. The Difference Fourier Technique in Protein Crystallography: Errors and Their Treatment. *Acta Crystallogr., Sect. B: Struct. Crystallogr. Cryst. Chem.* **1971**, *27*, 1414−1420.
(64) Coelho, A. A. Whole-Profile Structure Solution from Powder Diffraction Data Using Simulated Annealing. *J. Appl. Crystallogr.* **2000**, *33*, 899−908.
(65) Smeets, S.; McCusker, L. B.; Baerlocher, C.; Elomari, S.; Xie, D.; Zones, S. I. Locating Organic Guests in Inorganic Host Materials from X-Ray Powder Diffraction Data. *J. Am. Chem. Soc.* **2016**, *138*, 7099−7106.
(66) Kapoor, A.; Ritter, J. A.; Yang, R. T. On the Dubinin-Radushkevich equation for adsorption in microporous solids in the Henry's law region. *Langmuir* **1989**, *5*, 1118−1121.
(67) Schindler, B. J.; Buettner, L. C.; Douglas LeVan, M. Transition to Henry's law in ultra-low concentration adsorption equilibrium for n-pentane on BPL activated carbon. *Carbon* **2008**, *46*, 1285−1293.
(68) Ridha, F. N.; Webley, P. A. Anomalous Henry's law behavior of nitrogen and carbon dioxide adsorption on alkali-exchanged chabazite zeolites. *Sep. Purif. Technol.* **2009**, *67*, 336−343.
(69) Li, P.; Handan Tezel, F. Adsorption separation of N_2, O_2, CO_2 and CH_4 gases by β-zeolite. *Microporous Mesoporous Mater.* **2007**, *98*, 94−101.
(70) Patterson, T.; Esteves, S.; Dinsdale, R.; Guwy, A. An Evaluation of the Policy and Techno-Economic Factors Affecting the Potential for Biogas Upgrading for Transport Fuel Use in the UK. *Energy Policy* **2011**, *39*, 1806−1816.
(71) Grande, C. A.; Rodrigues, A. E. Biogas to Fuel by Vacuum Pressure Swing Adsorption I. Behavior of Equilibrium and Kinetic-Based Adsorbents. *Ind. Eng. Chem. Res.* **2007**, *46*, 4595−4605.
(72) Abatzoglou, N.; Boivin, S. A Review of Biogas Purification Processes. *Biofuels, Bioprod. Biorefin.* **2009**, *3*, 42−71.
(73) Yang, R. T. *Adsorbents Adsorbents: Fundamentals and Applications*; John Wiley & Sons, 2003.
(74) Delaval, Y.; Cohen de Lara, E. Study of physisorption of carbon dioxide on NAA zeolite. Part 1.-Experimental results obtained by infrared spectroscopy. *J. Chem. Soc., Faraday Trans.* **1981**, *77*, 869−877.
(75) Delaval, Y.; Seloudoux, R.; de Lara, E. C. Determination of isotherms and initial heat of adsorption of CO_2 and N_2O in four A zeolites from infrared measurements. *J. Chem. Soc., Faraday Trans. 1* **1986**, *82*, 365.
(76) Förster, H.; Schumann, M. Infrared spectroscopic studies on carbon dioxide adsorption in alkali-metal and alkaline-earth-metal ion-exchanged A-type zeolites. Part 1.-General features of CO_2 interaction with A-type zeolites. *J. Chem. Soc., Faraday Trans. 1* **1989**, *85*, 1149.
(77) Masuda, T.; Tsutsumi, K.; Takahashi, H. Infrared and Calorimetric Studies of Adsorbed Carbon Dioxide on NaA and CaNaA Zeolites. *J. Colloid Interface Sci.* **1980**, *77*, 232−237.
(78) Ward, J. W.; Habgood, H. W. The Infrared Spectra of Carbon Dioxide Adsorbed on Zeolite X. *J. Phys. Chem.* **1966**, *70*, 1178−1182.
(79) Kim, J.; Abouelnasr, M.; Lin, L.-C.; Smit, B. Large-Scale Screening of Zeolite Structures for CO_2 Membrane Separations. *J. Am. Chem. Soc.* **2013**, *135*, 7545−7552.
(80) Bertsch, L.; Habgood, H. W. An Infrared Spectroscopic Study of The Adsorption of Water and Carbon Dioxide By Linde Molecular Sieve X1. *J. Phys. Chem.* **1963**, *67*, 1621−1628.
(81) Galhotra, P.; Navea, J. G.; Larsen, S. C.; Grassian, V. H. Carbon dioxide ($C^{16}O_2$ and $C^{18}O_2$) adsorption in zeolite Y materials: effect of cation, adsorbed water and particle size. *Energy Environ. Sci.* **2009**, *2*, 401−409.
(82) Bondi, A. Van Der Waals Volumes and Radii. *J. Phys. Chem.* **1964**, *68*, 441−451.
(83) Lozinska, M. M.; Mowat, J. P. S.; Wright, P. A.; Thompson, S. P.; Jorda, J. L.; Palomino, M.; Valencia, S.; Rey, F. Cation Gating and Relocation during the Highly Selective "Trapdoor" Adsorption of CO_2 on Univalent Cation Forms of Zeolite Rho. *Chem. Mater.* **2014**, *26*, 2052−2061.
(84) Lozinska, M. M.; Mangano, E.; Greenaway, A. G.; Fletcher, R.; Thompson, S. P.; Murray, C. A.; Brandani, S.; Wright, P. A. Cation Control of Molecular Sieving by Flexible Li-Containing Zeolite Rho. *J. Phys. Chem. C* **2016**, *120*, 19652−19662.

DOI: 10.1021/acs.jpcc.8b09405
J. Phys. Chem. C 2018, 122, 27005−27015